

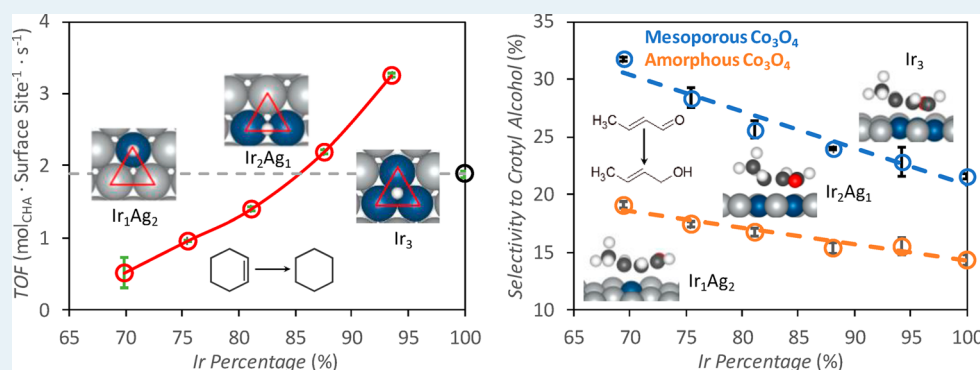
# Microwave-Assisted Synthesis of Classically Immiscible Ag–Ir Alloy Nanoparticle Catalysts

Hongyu Guo,<sup>†</sup> Hao Li,<sup>†</sup> Karalee Jarvis,<sup>‡,§</sup> Haiqin Wan,<sup>†,§</sup> Pranaw Kunal,<sup>†</sup> Samuel G. Dunning,<sup>†</sup> Yulu Liu,<sup>†</sup> Graeme Henkelman,<sup>\*,†,§</sup> and Simon M. Humphrey<sup>\*,†,§</sup>

<sup>†</sup>Department of Chemistry, The University of Texas at Austin, Welch Hall 2.204, 105 E 24th Street Stop A5300, Austin, Texas 78712-1224, United States

<sup>‡</sup>Texas Materials Institute, The University of Texas at Austin, 204 E. Dean Keeton Street Stop C2201, Austin, Texas 78712-1591, United States

## Supporting Information



**ABSTRACT:** We present the synthesis of Ag–Ir alloys in the form of solid-solution nanoparticles (NPs). Ag and Ir are classically immiscible in the bulk and therefore the physical properties of Ag–Ir alloys are unknown. A convenient microwave-assisted, solution-phase method that employs readily available Ag(NO<sub>3</sub>) and IrCl<sub>3</sub> precursors enables the preparation of small (2.5–5.5 nm) Ag–IrNPs with alloyed structures. Ag<sub>x</sub>Ir<sub>(100-x)</sub>NPs can be obtained by this method between  $x = 6–31$ . The Ag–IrNPs resist dealloying upon heating up to 300 °C. Ir-rich Ag–IrNPs dispersed on amorphous silica are significantly more active gas-phase alkene hydrogenation catalysts than pure IrNPs. Density functional theory (DFT) and theoretical modeling studies reveal that the Ag–IrNPs—which are consistently larger than monometallic IrNPs prepared under the same conditions—have comparatively fewer strong H-binding edge sites. This promotes faster H atom transfer to coadsorbed alkenes. Ag–IrNPs supported on amorphous Co<sub>3</sub>O<sub>4</sub> show a linear composition dependence in the selective hydrogenation of C=O versus C=C bonds: more Ag-rich Ag–IrNPs are more selective toward C=O hydrogenation of the  $\alpha,\beta$ -unsaturated aldehyde crotonaldehyde, yielding the industrially desirable crotyl alcohol. Furthermore, deposition of Ag–IrNPs inside Co<sub>3</sub>O<sub>4</sub> mesopores results in an additional ~56% selectivity enhancement.

**KEYWORDS:** metallic nanoparticles, alloy nanoparticles, microwave synthesis, heterogeneous catalysis, crotonaldehyde hydrogenation, silver, iridium

## INTRODUCTION

Iridium is an industrially important noble metal, yet it is also the scarcest noble metal found in the Earth's crust.<sup>1</sup> Organoiridium complexes are widely employed in homogeneous carbonylation catalysis (e.g., the BP-Cativa process<sup>2</sup>), and in OLED technology.<sup>3</sup> Heterogeneously, Ir is employed in NO reduction,<sup>4</sup> in CO and ammonia oxidation,<sup>5</sup> in water splitting,<sup>6</sup> in hydrazine decomposition,<sup>7</sup> and in the hydrogenation of aldehydes and nitrobenzenes,<sup>8</sup> for which Ir shows unrivalled selectivity. Metallic Ir is one of the most corrosion- and oxidation-resistant metals known, whose alloys with Os and Pt display extreme mechanical hardness.<sup>9</sup> For related reasons, the synthesis of size- and shape-controlled IrNPs is particularly problematic: its high melting point and resistance to surface

etching limits the size to which IrNPs can be grown. IrNPs tend to resist growth above ~2 nm, which limits their utility. There are several recent reports of synthetic procedures to obtain larger IrNPs, but these tend to rely on either the use of more exotic Ir precursors<sup>10</sup> or unusual solvents and coreductants<sup>11</sup>—neither of which are compatible with industrial-scale synthesis. Ir is also broadly immiscible in the bulk with other late transition metals, including Rh and the Group 11 metals.<sup>12</sup> However, nanoalloys of Ir with such metals would be potentially interesting for a number of reasons, including: (a) as a means to dilute the

Received: May 30, 2018

Revised: August 28, 2018

Published: October 3, 2018

amount of scarce Ir with more earth-abundant metals; (b) to access synergistic effects intrinsic to alloys (e.g., charge-transfer, ensemble, and strain<sup>13</sup> effects); and, (c) to enable better size and morphological control in the synthesis of Ir-based NPs. Yet, examples of Ir/M NPs in the literature remain rare. In recent work, Pd-IrNPs have been prepared and used to catalyze hydrazine decomposition and formic acid electrooxidation,<sup>14</sup> and Ni-IrNPs<sup>15</sup> were also reported.

We have become interested in forming Ir-based alloy MNPs with Group 11 metals, in the belief that a microwave- ( $\mu$ w-) assisted synthesis route under continued development in our lab<sup>16</sup> could enable the formation of well-defined metastable alloy nanostructures. We have previously shown that other classically immiscible bimetallics (e.g., Rh–Ag and Rh–Au<sup>16a</sup>) can be obtained as metastable NPs with randomly alloyed structures, by taking advantage of dipolar heating effects. Polar solvents and inherently polarizable ionic metal precursors strongly couple with  $\mu$ w irradiation. In turn, this results in rapid, localized heat dissipation.<sup>17</sup> This inhomogeneous heating leads to so-called “hotspot” formation, whereby localized regions of solution may become orders of magnitude hotter than the bulk solvent temperature for short periods of time.<sup>18</sup> These regions are thought to provide unique environments for NP nucleation and growth.

To the best of our knowledge, the synthesis of Ag–Ir alloys are previously unreported. Ag and Ir both adopt face-centered cubic (FCC) lattice structures and have similar lattice constants ( $a_{\text{Ag}} = 4.09$ ;  $a_{\text{Ir}} = 3.84$  Å); the 6% lattice mismatch between Ag and Ir should result in modest strain when mixed into a single phase, but should not inhibit alloy NP formation.<sup>19</sup> In this paper, we present the  $\mu$ w-assisted synthesis of  $\text{Ag}_x\text{Ir}_{(100-x)}$  bimetallic NPs with random alloy structures. With the aid of density functional theory (DFT) calculations, we have assessed the electronic structure of Ag–IrNP surfaces as a function of relative Ag:Ir composition, using model heterogeneous hydrogenation reactions as probes of surface reactivity. Given the major industrial uses of Ir, we chose to assess the selective hydrogenation properties of Ag–IrNPs. Both experiment and theory reveal that Ag–Ir alloys are more active hydrogenation catalysts than pure IrNPs, while the selectivity of C=C versus C=O bond hydrogenation is directly proportional to the Ag:Ir composition. DFT calculations elucidate that the observed trends in hydrogenation activity are correlated to both atomic ensemble and NP size effects.

## RESULTS AND DISCUSSION

**Microwave-Assisted Synthesis of  $\text{Ag}_x\text{Ir}_{(100-x)}$ NPs.**  $\text{Ag}_x\text{Ir}_{(100-x)}$ NPs with varying compositions were prepared by changing the relative molar amounts of  $\text{Ag}^+$  and  $\text{Ir}^{3+}$  precursors. Briefly, separate solutions of  $\text{Ag}(\text{NO}_3)$  and  $\text{IrCl}_3 \cdot n\text{H}_2\text{O}$  in ethylene glycol (EG) were directly coinjected into a stirred EG mixture containing *poly*(vinylpyrrolidone) (PVP; 9 monomers per total metal atom) held at 197 °C inside the cavity of a CEM-MARS-5 microwave reactor. The precursors were added at a combined rate of 2.0 mmol h<sup>-1</sup> (3 min total injection period) controlled by a dual-barrel syringe pump (see Supporting Information, SI, for further details). Deeply colored suspensions were obtained almost immediately, indicating rapid reduction of the metal precursors. The suspensions were heated for a further 30 min at 197 °C before being quenched in an ice water bath. A series of initial reactions were conducted to prepare  $\text{Ag}_x\text{Ir}_{(100-x)}$ NPs with nominal target compositions across the entire composition range,  $x = 8$ –92, in regular increments.

The isolated products were first analyzed by powder X-ray diffraction (PXRD) analysis to assess the extent of alloying

between Ag and Ir. Comparison of the PXRD patterns for the  $\text{Ag}_x\text{Ir}_{(100-x)}$ NPs to the corresponding patterns for pure Ag and IrNPs confirmed that Ag and Ir had become intrinsically alloyed into an FCC lattice arrangement, in all instances. The major (111), (200), and (220) reflections shifted as a function of changing Ag:Ir composition (Figure 1A). The (220) lattice spacings measured from the PXRD spectra showed good agreement versus calculated values obtained using Bragg's Law for all Ag–Ir compositions studied (Figure S2). These peaks were also broad, indicative of the formation of small nanostructures. The sizes of the Ag–Ir NPs can be calculated using the Scherrer equation; this indicates a consistent increase in size as a function of increasing Ag composition (Table 1). Notably, for all reactions with  $x > 42$ , a second set of more intense reflections began to appear, indicative of the coformation significantly larger monometallic AgNPs, in addition to the target Ag–IrNPs (Figure 1A;  $\text{Ag}_{50}\text{Ir}_{50}$  and  $\text{Ag}_{67}\text{Ir}_{33}$ ). Despite various attempts to modify the synthesis conditions to prevent partial segregation of Ag at higher  $\text{Ag}^+$  concentrations, we were only able to reproducibly access a single phase of Ag–IrNPs within the nominal range,  $x = 8$ –42 using the  $\mu$ w-assisted method. As observed previously,<sup>16,20</sup> the presence of  $\text{Cl}^-$  ions from the  $\text{Ir}^{3+}$  precursor also results in the formation of a minority of AgClNP byproducts, evidenced by additional reflections observed in the as-synthesized PXRD patterns (Figure S3). However, these AgClNPs were easily eliminated by treatment of the products with a few drops of concentrated  $\text{NH}_4\text{OH}$ , resulting in AgCl-free Ag–IrNPs (Figure 1A). Low-resolution transmission electron microscopy (TEM) images of the products obtained revealed that the  $\text{Ag}_x\text{Ir}_{(100-x)}$ NPs displayed a range of morphologies, whose average sizes (2.5–5.5 nm) lie between monometallic IrNPs (1.7 nm) and AgNPs (25 nm and larger) obtained by the same method (Figure S4); the Ag–IrNPs also became larger and less monodisperse with increasing Ag content (Figure 1B). The size analysis was conducted based on the measurement of at least 300 individual NPs from at least three separate areas of the same TEM grid.

Inductively coupled plasma optical emission spectroscopy (ICP-OES) and X-ray photoelectron spectroscopy (XPS) were next used to determine the bulk compositions of the purified Ag–IrNPs. Both methods were in close agreement for all compositions (Table 1 and Figure S6). On the basis of ICP-OES and XPS data, the actual NP compositions were all found to be ~27% deficient in Ag compared with the nominal targeted compositions (Figure S6). This indicates that the proportion of AgClNP byproducts formed was relatively consistent for all reactions. Henceforth, all  $\text{Ag}_x\text{Ir}_{(100-x)}$ NPs compositions in the work are quoted based on the actual compositions measured by ICP-OES analysis. XPS also confirmed that the majority of the Ir and Ag was present in the zerovalent state. The measured binding energy of the  $4f_{7/2}$  transition for Ir (ca. 60.9 eV) is indicative of  $\text{Ir}^0$ , while the  $3d_{5/2}$  transition for  $\text{Ag}^0$  (binding energy = 368.1 eV) are consistent with previous reports of metallic Ir and AgNPs (Figures S6–S10).<sup>15,16a</sup>

High-resolution (HR) TEM images of the most Ir-rich  $\text{Ag}_6\text{Ir}_{94}$ NPs showed lattice fringes corresponding to a [111] plane with a measured  $d$ -spacing of 2.23 Å, in close agreement with the  $d$ -spacing derived from the PXRD pattern using Bragg's Law (2.225 Å; Figure 2A). Line scanning energy-dispersive spectroscopy (EDS) of the same particles revealed the presence of both Ag and Ir in an even distribution and did not indicate segregation of metals between the NP cores and surfaces (Figure 2B). High-angle annular dark field scanning TEM (HAADF-STEM)

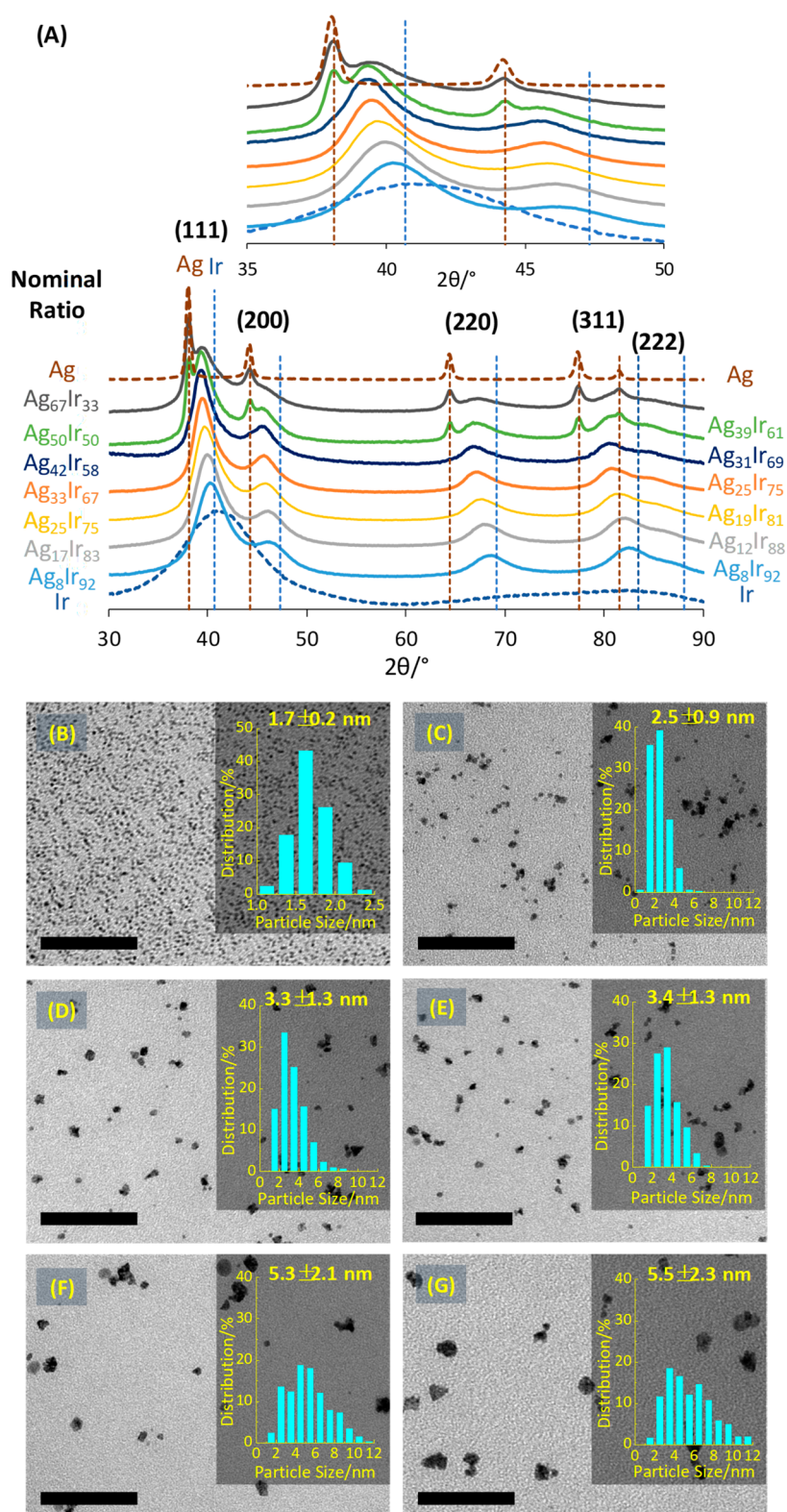


**Figure 1.** (A) PXRD patterns for Ag, Ir and  $\text{Ag}_x\text{Ir}_{(100-x)}$  NPs of different compositions; the corresponding theoretical reflection positions for Ag (JCPDS card # 01-087-0597) and Ir NPs (JCPDS card # 01-087-0715) are also shown for reference. Inset: magnification of the (111) and (200) reflections. (B–G) TEM images for pure Ir NPs and  $\text{Ag}_x\text{Ir}_{(100-x)}$  NPs with different compositions; insets: size distribution histograms. Scale bars equal to 50 nm.

imaging and 2-D elemental mapping analysis of a collection of three  $\text{Ag}_6\text{Ir}_{94}$  NPs also confirmed that Ag and Ir were evenly distributed throughout each particle (Figure 2C–F). Similarly, elemental mapping and EDS line scan analyses of other, more

Ag-rich Ag–Ir NPs were indicative of single-particle homogeneity (e.g.,  $\text{Ag}_{31}\text{Ir}_{69}$ ; Figure 3).

**Mechanistic Investigations into Microwave-Assisted Formation of  $\text{Ag}_x\text{Ir}_{(100-x)}$  NPs.** In an attempt to gain a better

Table 1. Physical Characterization of  $\text{Ag}_x\text{Ir}_{(100-x)}\text{NPs}$ 

nominal composition (%)		composition by IC-P-OES (%)		composition by XPS (%)		size (nm)	
Ag	Ir	Ag	Ir	Ag	Ir	PXRD	TEM
8	92	6	94	5	95	2.1	$2.5 \pm 0.9$
17	83	12	88	13	87	2.4	$3.3 \pm 1.3$
25	75	19	81	18	82	2.6	$3.4 \pm 1.3$
33	67	25	75	25	75	3.3	$5.3 \pm 2.1$
42	58	31	69	31	69	3.3	$5.5 \pm 2.3$

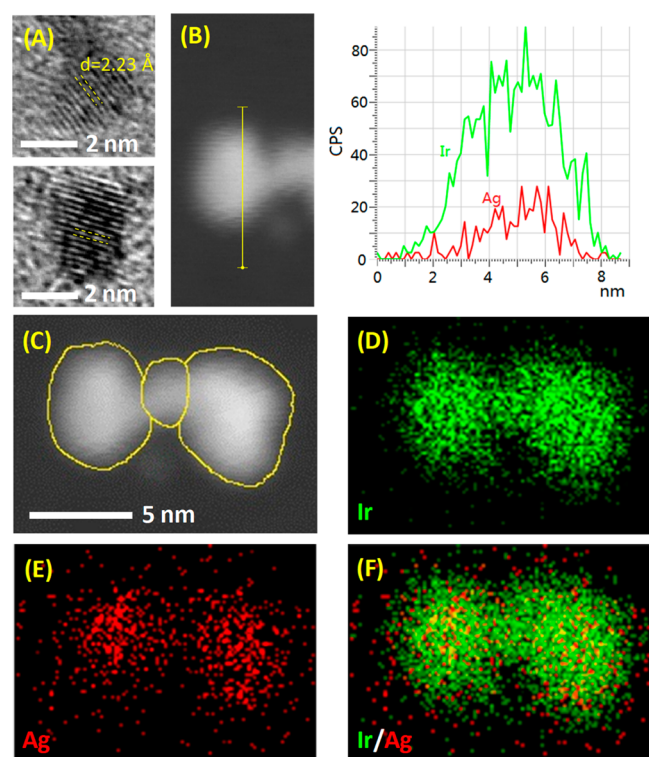


**Figure 2.** (A) Representative HR-TEM images for  $\text{Ag}_6\text{Ir}_{94}\text{NPs}$ , with the lattice spacing shown as yellow dashed lines. (B) Line-scan elemental profiling of a  $\text{Ag}_6\text{Ir}_{94}\text{NP}$  with corresponding elemental counts. (C) HAADF-STEM images for a collection of three  $\text{Ag}_6\text{Ir}_{94}\text{NPs}$ ; the corresponding 2-D EDS maps (Ir; green) (Ag; red) and the overlay map are shown in (D–F), respectively.

understanding of why only  $\text{Ag}_x\text{Ir}_{(100-x)}\text{NP}$  alloys with  $x \leq 31$  could be obtained in the absence of  $\text{AgNPs}$  under  $\mu\text{w}$  irradiation, the kinetics of alloying were assessed in the formation of NPs with intermediate composition ( $\text{Ag}_{19}\text{Ir}_{81}$ ). At early synthesis times (60 s, when only one third of the total metal precursors had been injected), aliquots were removed, flash-frozen to prevent further growth, and analyzed by PXRD. Very broad diffraction peaks were observed (Figure S12), indicating the existence of small nucleates. The (111) reflection maximum ca.  $39.5^\circ 2\theta$  corresponds to an FCC Ag–Ir alloy phase, but most notably, shoulders at lower  $2\theta$  values were also present, revealing the coexistence of small  $\text{AgNPs}$ . The reduction potential of  $\text{Ir}^{3+} \rightarrow \text{Ir}^0$  (1.156 V) is significantly higher than that of  $\text{Ag}^+ \rightarrow \text{Ag}^0$  (0.7991 V).<sup>21</sup> This suggests that  $\text{Ag}^+$  undergoes faster reduction than  $\text{Ir}^{3+}$  in solution, facilitated by the EG solvent. This would lead to the initial formation of monometallic Ag (or very Ag-rich) seeds, in agreement with the PXRD findings. Upon completion of metal precursor addition (180 s), further aliquots were removed and analyzed by PXRD. The reflections due to

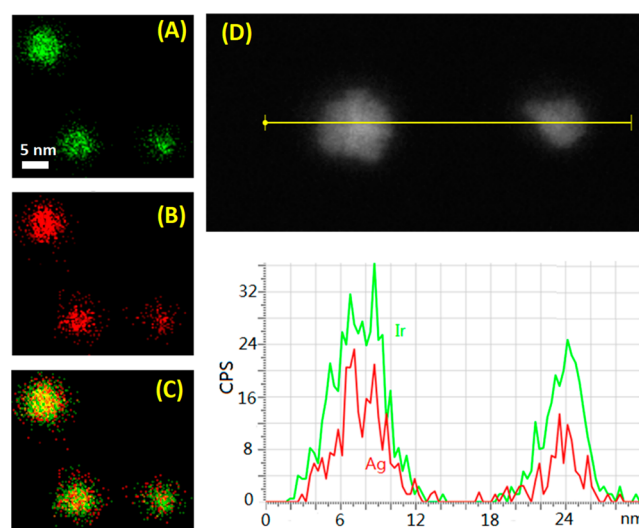


**Figure 3.** 2-D EDS maps of (A) Ir (green), (B) Ag (red), and (C) the overlay map of three  $\text{Ag}_{31}\text{Ir}_{69}\text{NPs}$ . (D) Line-scan elemental profiling of the bottom two  $\text{Ag}_{31}\text{Ir}_{69}\text{NPs}$  with corresponding elemental counts.

Ag–Ir were already narrower and the peak maxima had shifted to higher angles, indicative of the inclusion of more Ir into the growing particles, confirmed using the Scherrer eq (Table S3). The shoulders originally observed for pure Ag were also no longer visible (Figure S12). Galvanic replacement is energetically favored between  $\text{Ir}^{3+}$  and  $\text{Ag}^0$ ;<sup>22</sup>  $\text{Ir}^{n+}$  species are also autocatalytically reduced at the surfaces of Ag-rich nucleates.<sup>23</sup> Either (or both) of these processes are likely to lead to the absorption of Ir atoms into the growing NPs. Furthermore, when preformed  $\text{AgNPs}$  were treated with molecular  $\text{Ir}^{3+}$  under the same reaction conditions, Ag–Ir alloy NPs were obtained (Figure S13). PXRD analysis of the same NPs after a further 3 and 30 min of heating showed no obvious changes, indicating that all  $\text{Ir}^{3+}$  had been consumed almost immediately after completion of precursor addition.

The beneficial effects of  $\mu\text{w}$ -heating in the formation of Ag–IrNP alloys was also assessed by direct comparison to the products obtained by conventional (convective, oil bath) heating, using otherwise identical conditions and apparatus. Interestingly, conventionally heated reactions always yielded mixtures of Ag–Ir and pure  $\text{AgNPs}$  under conditions that cleanly yielded Ag–IrNPs by  $\mu\text{w}$ -assisted heating. The products from conventional reactions were also largely amorphous or poly crystalline, as indicated by PXRD and TEM analysis (Figures S14 and S15). These observations further support the hypothesis that localized superheated regions achieved under  $\mu\text{w}$  irradiation may be important in the formation of alloyed seeds, by ensuring faster incorporation of Ir atoms into the growing clusters. The observations are also in-line with what has been observed previously in the formation of Rh–Ag and Rh–Au alloy NPs.<sup>16a</sup> It is also expected that faster nucleation and growth under  $\mu\text{w}$  irradiation would lead to more crystalline Ag–IrNPs, as indicated by the significantly sharper diffraction peaks in the PXRD patterns.

The relative stability of the Ag–Ir alloys was also assessed as a function of temperature. The inherent immiscibility of Ag and Ir in the bulk should lead to the formation of metastable Ag–IrNP alloys, which would be expected to undergo segregation upon prolonged heating at elevated temperatures. To investigate this, isolated PVP-capped Ag–IrNPs of varying compositions were heated in the solid state using a tube furnace purged with  $\text{N}_2$  gas

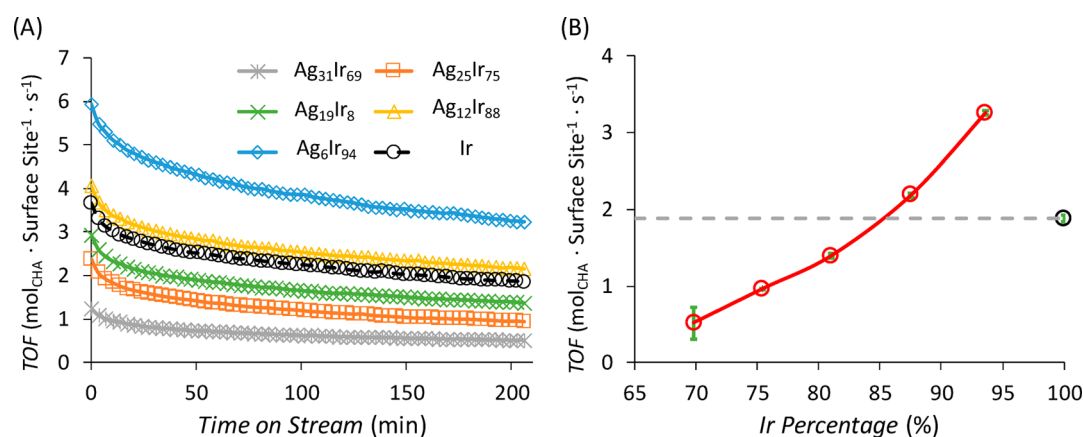


**Figure 4.** (A) Time-dependent TOF data for CHE hydrogenation catalyzed by Ag<sub>x</sub>Ir<sub>(100-x)</sub>NPs supported on *a*-SiO<sub>2</sub>, collected at 25 °C. The normalized reference TOF for an IrNP/*a*-SiO<sub>2</sub> catalyst is shown in black. (B) A plot of the measured TOFs at 200 min on-stream as a function of %Ir composition in the alloy NPs, compared to pure IrNPs (dashed gray line); and error bars were obtained by averaging TOF values for three separate batches of catalyst.

at 200, 250, 300, 325, 350, and 375 °C for 12 h. The resulting PXRD patterns clearly indicated that the NPs heated to 250 °C retained their alloy structures, and the onset of dealloying occurred at around 300 °C. The extent of dealloying is more obvious from the 2-D EDS maps of the thermally treated NPs, which indicate significant segregation of Ag and Ir (Figure S16). At 325 °C and higher temperatures, the PXRD peaks were much sharper indicating significant agglomeration. PVP is expected to thermally decompose at 380 °C,<sup>24</sup> so it should also be noted that NP agglomeration may accelerate Ag–Ir dealloying as larger NPs begin to mimic the bulk (Figures S18 and S19).

#### Assessment of Ag<sub>x</sub>Ir<sub>(100-x)</sub>NP Alloy Surface Reactivity via Model Vapor-Phase Hydrogenation Studies and DFT.

The vapor-phase hydrogenation of cyclohexene (CHE) to cyclohexane (CHA) by H<sub>2</sub> was used as a model reaction to study the catalytic properties of Ag<sub>x</sub>Ir<sub>(100-x)</sub>NPs as a function of *x*, and in comparison to monometallic AgNPs and IrNPs. This simple reaction was chosen as it enables convenient extraction of basic kinetic information that can be used to infer surface binding energies as a function of average surface composition. In our study, amorphous silica (*a*-SiO<sub>2</sub>) was employed as a chemically inert support that does not induce strong metal–support interactions. Deposition of Ag–IrNPs onto *a*-SiO<sub>2</sub> also enables easy catalyst handling and minimizes NP sintering under catalytic conditions. In each reaction, approximately 3 mg of the Ag–IrNP/*a*-SiO<sub>2</sub> composite catalysts with ca. 3% total metal loading was employed; the actual Ag and Ir %wt loadings were determined by ICP-OES (see Methods section and SI). The catalysts were activated under facile conditions to favor retention of alloy structures. Activation was achieved in flowing H<sub>2</sub>/He at 25 °C for 30 min. Under these conditions, it has been shown that the NP surface atoms become reduced and residual PVP is released from the NP surfaces.<sup>16,21</sup> While the majority of PVP is still assumed to be present, the reactants (CHE and H<sub>2</sub>) can readily access the NP surfaces. The products were monitored in real-time by continuous on-stream sampling at 3.5 min intervals by gas chromatography.

The normalized turnover frequencies (TOFs; mol<sub>CHA</sub> · total metal surface site<sup>-1</sup> · s<sup>-1</sup>) of the supported Ag<sub>x</sub>Ir<sub>(100-x)</sub>NPs were obtained by normalization of apparent activities in terms of average NP size and morphology (see SI). As shown in Figure 4A, the measured TOFs were initially high upon exposure of the fully pre-reduced catalysts to CHE, but rapidly decayed (48 ± 6% of the

initial values after 200 min on-stream). As reported in previous literature,<sup>16a</sup> we also reconfirmed that similarly sized AgNPs supported on the same *a*-SiO<sub>2</sub> supports were inactive hydrogenation catalysts due to the inability of Ag to oxidatively add H<sub>2</sub> under the reaction conditions. Interestingly, however, the addition of relatively small amounts of Ag to Ir in the Ag–IrNPs (*x* < 12; Figure 4A) resulted in a significant increase in the measured TOFs compared to the reference TOF for monometallic IrNPs (Figure 4A) at 200 min on stream. In fact, the most Ir-rich Ag–Ir alloy (Ag<sub>6</sub>Ir<sub>94</sub>, blue diamonds; Figure 4) gave a TOF that was ca. 75% higher than for pure IrNPs. In general, the TOFs for alloys of varying compositions were directly dependent on *x*, with increasingly Ir-deficient NPs giving consistently lower activities; alloy NPs with *x* ≥ 19 were all less active than Ir itself (Figure 4B).

The recyclability of the supported Ag<sub>x</sub>Ir<sub>(100-x)</sub>/*a*-SiO<sub>2</sub> catalysts was also assessed for all compositions by twice regenerating each catalyst in flowing H<sub>2</sub>/He followed by re-exposure to CHE. This recovered the initially higher TOFs, while the TOFs obtained after three cycles were always less than 10% lower than the values obtained for the pristine catalysts (Figure S20). TEM analysis of the supported catalysts after three cycles revealed no obvious NP size or morphological changes (Figure S21).

In an attempt to elucidate the TOF trends shown in Figure 4, theoretical H-binding energies were calculated on model Ag<sub>x</sub>Ir<sub>(100-x)</sub> (111) surfaces as a function of *x*, using DFT. The results provide useful reaction descriptors that can be directly compared with the experimental CHE hydrogenation results. Figure 5A shows the calculated H-binding energies at four different triatomic ensembles (Ag<sub>3</sub>, Ir<sub>1</sub>Ag<sub>2</sub>, Ir<sub>2</sub>Ag<sub>1</sub>, and Ir<sub>3</sub>) on random alloy slabs of Ag<sub>25</sub>Ir<sub>75</sub>. Similar results were obtained for Ag<sub>10</sub>Ir<sub>90</sub>, Ag<sub>15</sub>Ir<sub>85</sub>, Ag<sub>30</sub>Ir<sub>70</sub>, and Ag<sub>40</sub>Ir<sub>60</sub> (Figure S23a–d). A triatomic ensemble with 3-fold geometry is the smallest repeat unit on an ordered (111) atomic surface that can be used to describe the local adsorption environment of H atoms.<sup>25</sup> Therefore, we focused on this binding site as a means to gain a theoretical understanding of the observed catalytic reactivity. The calculations show that, for Ir(111), both the 3-fold hollow and atop sites have similar favorable H binding energies (Figure 5A; yellow and purple dashed lines). Meanwhile, DFT predicts that the binding of an H atom at an Ag<sub>3</sub> site is much weaker than at the other three triatomic ensembles (Figure 5B). The binding is significantly weaker than –0.4 eV, which is the energy corresponding to the peak in the

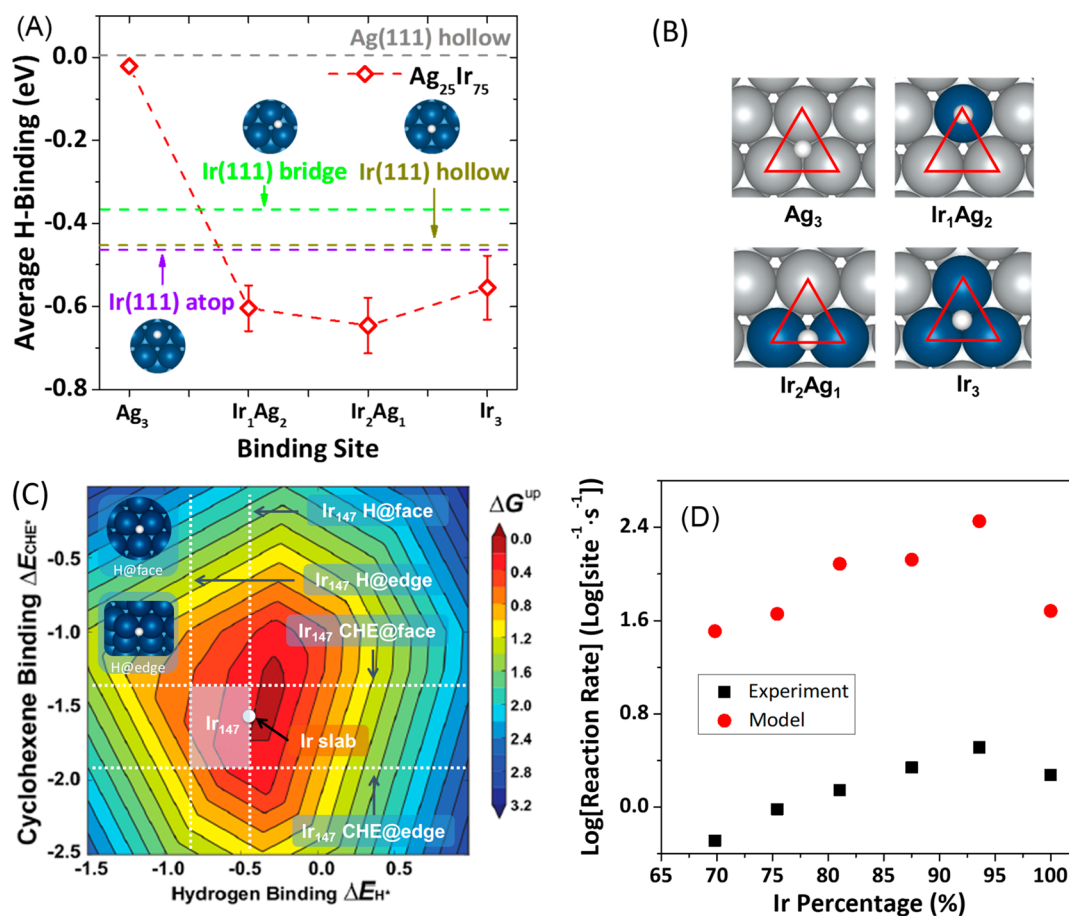


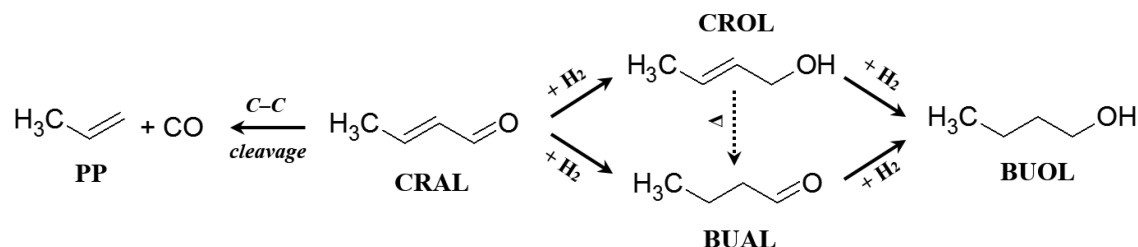
**Figure 5.** (A) Calculated binding energies of H atoms at different triatomic ensembles on  $\text{Ag}_{25}\text{Ir}_{75}$  slab surfaces. Standard deviations were calculated from ten binding sites on ten random alloys. Calculated H binding energies at atop (purple), bridge (green), and hollow (yellow) sites on pure  $\text{Ir}(111)$  surface and hollow site on pure  $\text{Ag}(111)$  surface (gray) are shown for comparison. Insets: the optimal geometries of H atom adsorption (white atoms). (B) Optimal positions of H atom calculated at four different triatomic ensembles ( $\text{Ag}_3$ ,  $\text{Ir}_1\text{Ag}_2$ ,  $\text{Ir}_2\text{Ag}_1$ , and  $\text{Ir}_3$ ). The blue, gray and white spheres represent Ir, Ag, and H atoms, respectively. (C) Calculated H- and CHE-binding energies on a model  $\text{Ir}(111)$  slab, and on an  $\text{Ir}_{147}\text{NP}$ . The data is plotted on a contour map showing  $\Delta G^{\text{up}}$  as a function of the binding energy of CHE and H. The binding energies on  $\text{Ir}_{147}$  were calculated on (111) face and edge sites, respectively. Insets: the optimized geometries of H adsorption (drawn in white). (D) Theoretical (red) and experimental (black) reaction rates of the Ag-Ir NPs with varying compositions.

volcano plot (Figure 5C). This finding is consistent with the inability of AgNPs to catalyze alkene hydrogenation. Details of the model used to calculate the volcano plot can be found in prior work.<sup>16</sup> When the proportion of Ir atoms is increased in a triatomic ensemble, the H atom binding affinity also increases to a point at which the binding is stronger than optimal, resulting in less labile H atoms. The calculated surface segregation energies of two isolated Ir atoms shows that thermodynamically, formation of larger Ir ensembles is more favorable (Figure S23e). Our calculations suggest that the Ag-Ir alloy system is best described as “untunable” for H atom binding, meaning that varying the relative Ag:Ir composition to change the proportion of mixed-metal surface ensembles does not provide access to intermediate H-binding energies. As we have seen previously with Pt-Au alloys,<sup>26</sup> the constant H-binding strength calculated for the Ag-Ir alloys is due to the fact that the H binding modes are actually different for each type of 3-atom ensemble found on a (111) surface (Figure 5B). H atoms preferentially bind at the 3-fold hollow site in an  $\text{Ir}_3$  ensemble, in a two-fold bridging orientation on  $\text{Ir}_2\text{Ag}_1$ , and to an Ir atop site in an  $\text{Ir}_1\text{Ag}_2$  ensemble (Figure 5B). This Ir-driven H atom migration behavior maintains an approximately constant H-binding energy at the Ag-IrNP surfaces. Accordingly, CHE-binding energies were

found to be similar to that of the pure  $\text{Ir}(111)$  surface (Table S5); alloying of Ag into Ir simply dilutes the Ir and is not predicted to improve the activity of CHE hydrogenation. This is entirely consistent with the experimental observation that the average TOF decreases somewhat linearly with decreasing Ir composition (Figure 4B). To physically understand the tuning of H-binding, our models for  $\text{Ir}(111)$  and  $\text{Ag}_{25}\text{Ir}_{75}(111)$  slabs were compared with an  $\text{Ir}(111)$  slab having its strain expanded to be the same as for bulk  $\text{Ag}_{25}\text{Ir}_{75}$  (Table S7). The surface strain did not change to any significant extent, but the calculated H-binding energies were found to be quite different between bulk  $\text{Ag}_{25}\text{Ir}_{75}$  and an expanded  $\text{Ir}(111)$  surface. This indicates that for Ag-Ir, both ensemble and electronic effects clearly influence the H-binding energies, while strain effects are much less significant.

In the above calculations, a slab model was used; this model is appropriate for the faces of the larger 2.5–5.5 nm  $\text{Ag}_x\text{Ir}_{(100-x)}$  NPs, but breaks down for the smallest 1.7 nm IrNPs. For those, we used a cuboctahedral Ir nanocluster consisting of 147 atoms, corresponding to a diameter of 1.9 nm. Figure 5C shows the calculated H- and CHE-binding energies obtained for both the  $\text{Ir}(111)$  slab and the  $\text{Ir}_{147}\text{NP}$ , overlaid onto the reaction activity volcano plot. This analysis shows that an  $\text{Ir}(111)$  slab is close to the volcano peak. In contrast, for an  $\text{Ir}_{147}\text{NP}$ , although the

Scheme 1. Most Common Reaction Outcomes in the Hydrogenation of Crotonaldehyde



binding of H on face sites is nearly optimal, the CHE binding is comparatively weaker than for an Ir (111) slab. The Ir<sub>147</sub> edge sites are predicted to overbind both H and CHE. Thus, the theoretical hydrogenation activity of Ir<sub>147</sub>NPs is predicted to be driven far away from the volcano peak due to the presence of more edge-binding sites; consequently, this lowers the catalytic activity due to slower release of the bound species. As a result, the catalytic activity of small IrNPs is predicted to be significantly lower than for larger, Ir-rich Ag<sub>x</sub>Ir<sub>(100-x)</sub>NPs. Interestingly, it is observed in Figure 5C that the H binding calculated on the (111) face of an Ir<sub>147</sub>NP is similar to that for an extended Ir(111) surface. Ir<sub>147</sub>NPs should display strong compressive strain due to surface tension effects at the nanoscale, which should lead to weaker H binding; conversely, the lower average coordination number of Ir atoms at the surfaces of Ir<sub>147</sub>NPs should strengthen the H-binding. These two opposing effects can thus lead to a similar final H-binding energy, as calculated on Ir(111). It should also be noted that under experimental conditions, the NP surfaces will have a certain (partial) coverage of H atoms; calculating the phase diagram of adsorbates under varying experimental conditions could help to more comprehensively evaluate the observed reaction activity, and will be studied in future work. Since H-binding energy has been found to be relatively insensitive to the total H atom coverage on Ir(111) (see Table S8), it can be assumed that these effects may be subtle.

To provide a straightforward evolution of our theoretical approach, we next developed a microkinetic model that unifies both Ag–Ir alloying and NP size effects. Figure 5D shows the estimated relative reaction rates at the NP surfaces with varying Ag:Ir compositions, while also considering the adsorption coverage, NP size, active site ratio, and total number of surface sites. It can be seen from this unified model that the trend of relative reaction rates has good qualitative agreement with the experimental trend in measured TOFs, shown in Figure 4B. This helps to further confirm that the theoretical approach employed in this work to deal with both H-tunability and NP size effects is able to accurately explain the experimental observations.

In this instance, experiment and theory both concur that the premise, “smallest is best” does not apply. Synthetically, the addition of small amounts of Ag into IrNPs allows for the preparation of physically larger NPs. Reactivity-wise, larger NPs have a greater proportion of more weakly binding surface sites versus more strongly binding edge sites, and the average binding energies of all mixed Ag/Ir surface ensembles are also weaker than those of pure Ir<sub>3</sub> ensembles. Therefore, the larger Ag–IrNPs provide more labile reaction intermediates for alkene hydrogenation, while also requiring physically less Ir in their manufacture.

**Selective C=O Hydrogenation by Ag<sub>x</sub>Ir<sub>(100-x)</sub>NPs.** Next, the catalytic properties of supported Ag<sub>x</sub>Ir<sub>(100-x)</sub>NPs as a direct function of *x* was studied using a more complicated model

hydrogenation reaction. Specifically, we assessed the relationships between Ag/Ir composition and the nature of the catalyst support upon the selective hydrogenation of the  $\alpha,\beta$ -unsaturated aldehyde, crotonaldehyde (CRAL; Scheme 1). There are several possible outcomes in the vapor-phase hydrogenation of CRAL, illustrated in Scheme 1. From a technological standpoint, selective hydrogenation of the aldehyde C=O moiety is desired, yielding the industrially valuable unsaturated crotyl alcohol (CROL). Conversely, hydrogenation of the C=C bond is thermodynamically favored,<sup>27</sup> but the resulting saturated butyraldehyde (BUAL) is worthless since it can already be made easily on a large scale by homogeneous hydroformylation chemistry.<sup>3</sup> Overhydrogenation to give butanol (BUOL) or C–C cleavage to give propene (PP) are also undesirable and are more commonly observed under more forcing reaction conditions. Others have shown that noble metal NPs supported on particular transition metal oxides can impart the desired selectivity.<sup>28,29</sup> For example, AuNPs supported on TiO<sub>2</sub> are able to achieve ~65% selectivity toward CROL at 120 °C, with a partial pressure of 8 Torr for crotonaldehyde.<sup>28a</sup> The origins of selectivity in this reaction are manifold; in addition to H<sub>2</sub> activation by a noble metal, H-spillover and preferential orientation effects of CRAL at the support surface are known to be important.<sup>28b</sup> Recently, Somorjai and co-workers proposed that the hydrogenation selectivity of CRAL achieved by monometallic PtNPs deposited on a Co<sub>3</sub>O<sub>4</sub> film was directly dependent on the structure of the support.<sup>29</sup> Specifically, they found that hydrogenation of the C=C bond occurred by direct coadsorption of H<sub>2</sub> and CRAL on the PtNP surfaces, akin to the mechanism responsible for the hydrogenation of CHE described above. Meanwhile, the desired C=O bond hydrogenation occurred primarily on the surface of the Co<sub>3</sub>O<sub>4</sub> support. Using in situ sum-frequency generation (SFG) vibrational spectroscopy, it was shown that CRAL molecules were preferentially adsorbed in a “head-on” C=O⋯Co orientation, thus activating the C=O bond and allowing hydrogenation to yield the unsaturated alcohol localized at the support.

Taking a lead from these recent results, and based on our preliminary hydrogenation studies with the Ag–IrNP catalysts described above, we were interested to see if Ag–Ir alloys showed a composition dependence in the selective hydrogenation of CRAL in the vapor phase. In initial studies, activated *a*-SiO<sub>2</sub>-supported Ag<sub>x</sub>Ir<sub>(100-x)</sub>NPs catalysts (*x* = 6–31) were exposed to CRAL in the presence of H<sub>2</sub> gas. Unlike for CHE hydrogenation, the presence of PVP capping agents hindered the hydrogenation of CRAL and required more effective removal. This was achieved by pretreating the catalysts in flowing H<sub>2</sub>/He at 200 °C for 12 h before cooling to the reaction temperature of 90 °C. Under these moderately more forcing activation conditions, TEM analysis confirmed that the supported Ag–IrNPs remained unsintered (Figure S24). The aforementioned temperature-dependent studies also confirm that the Ag–IrNPs resist dealloying at this temperature. Additional PXRD

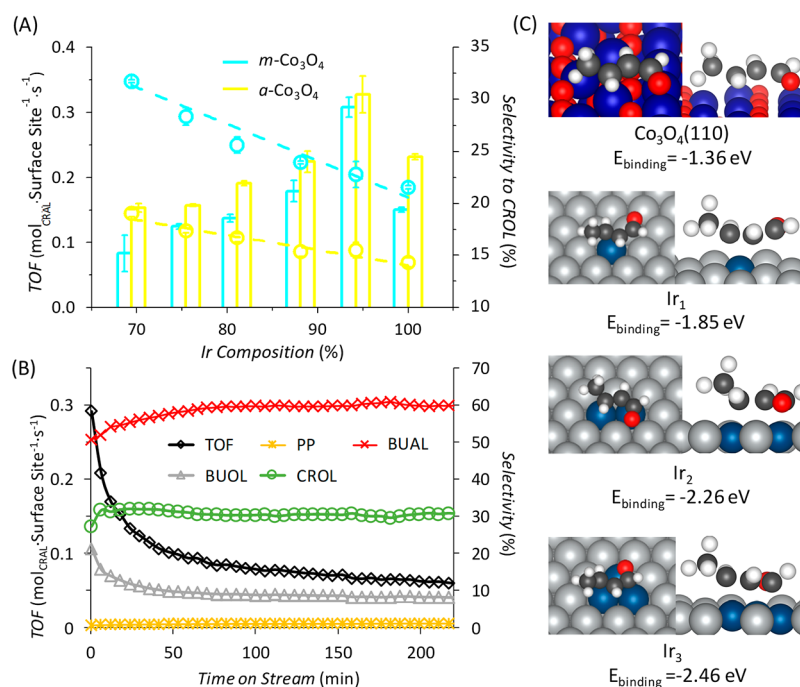


**Figure 6.** (A) The TOF and selectivity to crotyl alcohol obtained on Ag<sub>x</sub>Ir<sub>(100-x)</sub>/*a*-Co<sub>3</sub>O<sub>4</sub> (yellow) and Ag<sub>x</sub>Ir<sub>(100-x)</sub>/*m*-Co<sub>3</sub>O<sub>4</sub> (cyan), as a function of Ir percentage. (B) Time-dependent TOF (black diamonds) and corresponding selectivity data for CRAL hydrogenation, catalyzed by Ag<sub>31</sub>Ir<sub>69</sub>NPs supported on *m*-Co<sub>3</sub>O<sub>4</sub>. (C) The most favorable binding configurations and binding energies of CRAL on the (110) surface of Co<sub>3</sub>O<sub>4</sub>, and on Ir<sub>1</sub>, Ir<sub>2</sub> and Ir<sub>3</sub> NP surface ensembles, calculated by DFT. [Key: Ir = turquoise; O = red; C = black; H = white; Co = navy; Ag = gray].

studies of the catalysts reduced under these conditions did not reveal any new reflections that could be attributed to H<sub>2</sub> adsorbate-driven NP restructuring or segregation (Figure S25). 2-D EDS mapping of the catalyst after activation also showed that the NPs remained alloyed (Figure S26). Disappointingly, all of the alloy catalysts as well as an IrNP control catalyst supported on *a*-SiO<sub>2</sub> only yielded BUAL at low activity, in addition to barely detectable amounts of PP; neither CROL nor BUOL were observed, indicating that the C=O bond was not activated by these catalysts (Table S9 and Figures S27 and S28). Similar results were also obtained when  $\alpha$ -Al<sub>2</sub>O<sub>3</sub> was employed as a support in place of *a*-SiO<sub>2</sub>.

In stark contrast, when the Ag<sub>x</sub>Ir<sub>(100-x)</sub>NPs were deposited onto amorphous Co<sub>3</sub>O<sub>4</sub> at a metal loading of ca. 2 wt % and activated under otherwise identical conditions as those described above, the target CROL was obtained as a major product, in addition to BUAL and minor amounts of PP and BUOL (Figure 6A; yellow data). In agreement with the earlier Somorjai work, it is apparent from our results that Co<sub>3</sub>O<sub>4</sub> plays a crucial role in the activation of C=O groups. Importantly, the observed selectivity toward CROL was found to be sensitive to the Ag<sub>x</sub>Ir<sub>(100-x)</sub>NP composition. As shown in Figure 6A, the highest selectivity for CROL was obtained for the most Ag-rich NP catalyst (19.1%; Ag<sub>31</sub>Ir<sub>69</sub>), with a linear decrease in selectivity toward mono-metallic IrNPs (14.3%). This is both an interesting and potentially very important observation, since the greatest selectivity toward the desired CROL product is obtained for the most Ir-economical catalysts. The observation is also neatly explained by the experimental and DFT results obtained from the earlier CHE hydrogenation studies, based on three synergistic factors. (1) More Ag-rich Ag–IrNPs display surfaces with a greater proportion of weaker H-binding sites, which should promote faster H atom spillover on to the *a*-Co<sub>3</sub>O<sub>4</sub> support. (2) Increasingly Ag-rich Ag–IrNPs are predicted by DFT to be less active in the

direct hydrogenation of C=C bonds since a greater proportion of Ir surface sites have been substituted by Ag atoms, which are weaker C=C-binding sites. (3) The most Ag-rich NPs are also the largest NPs and display a greater ratio of weaker (surface) versus stronger (edge) C=C adsorption sites; therefore, direct C=C hydrogenation processes occurring on the largest NPs should be further disfavored versus indirect hydrogenation of C=O bonds on the neighboring supports. Similar to CHE hydrogenation, a decrease in TOF was observed with increasingly Ag-rich Ag–IrNPs.

Clearly, *a*-Co<sub>3</sub>O<sub>4</sub> plays a vital role in imparting desirable selectivity for this reaction. Yet a potentially even more important and previously unexplored factor has been uncovered in this study: the selectivity for CROL can be increased by over 56 ± 7% across the entire Ag–IrNP composition range by using a mesostructured (*m*-) version of Co<sub>3</sub>O<sub>4</sub> (Figure 6A; cyan data). We used a previously reported nanocasting method to obtain *m*-Co<sub>3</sub>O<sub>4</sub> with CMK-3 structure (hexagonally bundled rods), using SBA-15 as a sacrificial hard templating agent (SI Methods and Figures S29 and S30).<sup>30</sup> PXRD of the as-synthesized *m*-Co<sub>3</sub>O<sub>4</sub> was used to confirm phase purity (Figure S31), while bulk textural analysis performed by N<sub>2</sub> physisorption (78 K) yielded a BET<sup>31</sup> surface area of 55.8 m<sup>2</sup> g<sup>-1</sup> and a range of pore diameters between 3.3–9.0 nm (BJH method;<sup>32</sup> Figures S33 and S34). TEM analysis of the *m*-Co<sub>3</sub>O<sub>4</sub> materials revealed ordered pore structures in a great majority of particles (Figure S29). The predicted pore size should be large enough to accommodate the Ag–IrNPs made in this study. Incipient wetness impregnation of the NPs into the supports in an EtOH:H<sub>2</sub>O (v:v = 1:1) solvent mixture followed by sonication (20 min) resulted in the NPs becoming isolated inside the mesopores, which was confirmed using Z-contrast TEM (Figure S35). Upon activation under conditions identical to those used for *a*-Co<sub>3</sub>O<sub>4</sub>-supported catalysts, the selectivity to CROL by Ag<sub>31</sub>Ir<sub>69</sub>/*m*-Co<sub>3</sub>O<sub>4</sub> was 31.7%

(cf. 19.1% for  $\text{Ag}_{31}\text{Ir}_{69}/a\text{-Co}_3\text{O}_4$ ; Figure 6A). A similar magnitude of increasing selectivity toward CROL was observed for all other NP compositions. A plot of the time-dependent product selectivity for the most selective catalyst ( $\text{Ag}_{31}\text{Ir}_{69}/m\text{-Co}_3\text{O}_4$ ) is shown in Figure 6B, which confirms that the product distribution does not change with time-on-stream, or with decreasing TOF. A survey of the literature suggests that the best previous CROL selectivity obtained by Ir in the gas phase was only 23%, achieved by  $\text{ZrO}_2$ -supported IrNPs at a slightly higher reaction temperature (100 °C).<sup>33</sup> These Ag–Ir/ $m\text{-Co}_3\text{O}_4$  catalysts also showed very good recyclability: very little decrease in selectivity to CROL was observed after 5 cycles of catalysis and reactivation in  $\text{H}_2/\text{He}$  (Figure S37).

The hydrogenation selectivity of CRAL was investigated with DFT calculations of the binding energies on  $\text{Co}_3\text{O}_4$  (110) and the three (111) ensembles,  $\text{Ir}_3$ ,  $\text{Ir}_2\text{Ag}_1$ , and  $\text{IrAg}_2$  (Figure 6C). Due to the high computational cost required to accurately calculate Co-related systems, in this work we decided to evaluate reagent binding configurations and their energies, as opposed to detailed reaction kinetics. The thermodynamically most favorable binding configurations for the  $\text{Ir}_1$  and  $\text{Ir}_2$  ensembles indicate that CRAL is preferentially directly adsorbed to the Ag–IrNP surfaces via classical C=C bonding modes (Figure 6C). This type of interaction leads to direct C=C bond hydrogenation in the presence of coadsorbed H, and is insensitive to the nature of the support. Meanwhile, on larger Ir ensembles (e.g.,  $\text{Ir}_3$ ), CRAL is stabilized by adsorption of both C=C and C=O groups, which could result in hydrogenation of either (or both) bonds. Overall, these results indicate that on small Ir ensembles, C=C activation is favorable, while the activation of C=C and C=O are more equivalent on larger Ir ensembles. Perhaps more importantly, we also find that the most favorable adsorption mode for CRAL directly at the  $\text{Co}_3\text{O}_4$  (110) support is via an  $\eta^4\text{-}(\text{C},\text{C},\text{C},\text{O})$  mode, which is likely to result in selective hydrogenation of the C=O bond.<sup>27</sup> In agreement with the SFG results reported by Somorjai, the DFT studies conducted here help to explain why CROL is observed in significant quantities using  $\text{Co}_3\text{O}_4$  as a support. More Ir-rich Ag–IrNP surfaces favor C=C activation, while more Ag-rich alloys still facilitate  $\text{H}_2$  dissociation, to facilitate selective C=O hydrogenation at the NP-support interfaces.

The observed selectivity enhancement obtained using  $m\text{-Co}_3\text{O}_4$  as a support also reinforces the supposition that CRAL-support orientation effects play an important role in selective C=O activation: the  $m\text{-Co}_3\text{O}_4$  support has mesopores that are large enough to accommodate the  $\text{Ag}_x\text{Ir}_{(100-x)}$ NPs, but once loaded inside the mesopores (vide supra), there will be limited space for the passage of reagents (e.g., bottlenecks). Thus, the binding of CRAL at  $\text{Ag}_x\text{Ir}_{(100-x)}$ NP surfaces inside the mesopores via a side-on C=C binding mode should be more difficult to achieve than via a head-on C=O binding mode. In turn, this should reduce the selectivity toward butyraldehyde formation. Also, the mesoporous support should lead to slower diffusion of CRAL through the pores (due to mass-transport effects), which is likely to lead to a longer overall contact time. This should increase the chance of indirect C=O hydrogenation by spillover H atoms from the  $\text{Co}_3\text{O}_4$  support, thus further increasing the selectivity toward the unsaturated alcohol product.<sup>27</sup> Meanwhile, it should not be discounted that the surface states of  $\text{Co}_3\text{O}_4$  may differ between the amorphous and mesoporous forms. The  $\text{Co}_3\text{O}_4$ -supported composite catalysts were also studied by XPS in their as-synthesized, activated, and postcatalytic states (Figures S40). Upon activation of the catalysts under  $\text{H}_2$  at 200 °C, the

$m\text{-Co}_3\text{O}_4$  (Co(II)/(III)-containing) supports underwent partial reduction, presumably due to H-spillover, indicated by the emergence of new satellite peaks corresponding to CoO (Figure S40). However, measurable signals that could be attributed to either Co(I) or Co(0) were not observed, which rules out the possibility of the formation of trimetallic Co–Ag–IrNPs, or of isolated CoNPs on the supports.

## CONCLUSIONS

We have shown that small (2.5–5.5 nm) Ag–IrNPs with randomly alloyed structures can be prepared using a convenient microwave-assisted polyol method. The previously unstudied Ag–Ir nanoalloys were found to be active heterogeneous hydrogenation catalysts, which retain their alloy structures up to 300 °C. Addition of Ag to FCC–IrNPs enables the formation of physically larger NPs. DFT and modeling studies concur with experimental results and suggest that a greater proportion of surface Ir sites to edge sites in larger Ag–IrNPs results in a greater proportion of more weakly bound H atom intermediates, ultimately enabling more rapid catalysis.  $\text{Ag}_x\text{Ir}_{(100-x)}$ NPs with compositions  $x \geq 85$  were found to be more highly active alkene hydrogenation catalysts than pure IrNPs. Meanwhile, increasingly Ag-rich  $\text{Ag}_x\text{Ir}_{(100-x)}$ NPs are increasingly selective in the hydrogenation of C=O versus C=C bonds in crotonaldehyde, when supported on  $\text{Co}_3\text{O}_4$ . The unique reactivity of Ag–Ir nanoalloys found in this work is both interesting and complex, based on an interplay of NP size, ensemble and support effects. Ag–IrNPs are promising as a convenient means to fine-tune the reactivity of Ir catalysts for industrially relevant reactions, while also reducing the total amount of Ir required by dilution with Ag.

## MATERIALS AND METHODS

**Materials.** Iridium trichloride hydrate ( $\text{IrCl}_3 \cdot n\text{H}_2\text{O}$ , 100%; Johnson Matthey), silver nitrate ( $\text{AgNO}_3$ ,  $\geq 99.9\%$ ; Alfa Aesar), ethylene glycol ( $\{\text{CH}_2\text{OH}\}_2$ , 99.8%; Fisher Scientific), poly(vinylpyrrolidone) (PVP,  $\langle M_w \rangle = 58\,000$ ; Alfa Aesar) and ammonium hydroxide ( $\text{NH}_4\text{OH}$ , 28–30%; Fisher Scientific), were used as-received. The catalysis reagents 1-cyclohexene (CHE,  $\text{C}_6\text{H}_{10}$ , 99%+; Alfa Aesar) and crotonaldehyde (CRAL,  $\text{C}_4\text{H}_8\text{O}$ , 99.5%+, predominantly trans; Aldrich) were stored over 4A molecular sieves under dry  $\text{N}_2$  and were purged with  $\text{H}_2/\text{He}$  prior to use. All other common reagents and solvents (analytical grade) were used without further purification.

**Experimental Section.** Ag–IrNPs with different compositions were synthesized using a modified polyol method. In all reactions, PVP was predissolved in ethylene glycol and heated to 197 °C with magnetic stirring (450 rpm) inside a 50  $\text{cm}^3$  glass round-bottomed flask fitted with a cold water reflux condenser. The entire apparatus was placed inside the cavity of a CEM-MARS-5 microwave reactor with two parallel Teflon cannulas (I.D. = 1.0 mm) inserted down the condenser such that the metal precursor solutions were delivered directly above the stirred solution in the flask. Required amounts of  $\text{IrCl}_3$  and  $\text{AgNO}_3$  dissolved in 2.5 mL EG were injected into the reaction system a rate of 100  $\text{cm}^3 \text{h}^{-1}$  controlled by a dual-barrel syringe pump. The reaction mixture was heated for a further 30 min after injection to reach completion under microwave irradiation, followed by immediate quenching in an ice–water bath. The resulting  $\text{Ag}_x\text{Ir}_{(100-x)}$ NP suspensions were precipitated by addition of excess acetone and separated by centrifugation. The solids were washed with concentrated  $\text{NH}_4\text{OH}$  to remove

residual AgCl. To remove any excess PVP, the products were twice redispersed in a minimal amount of ethanol followed by precipitation with excess hexanes and isolated by centrifugation. The NPs were then dried under vacuum and stored in the form of amorphous glass.

Amorphous silica ( $a\text{-SiO}_2$ ) and amorphous cobalt oxide ( $a\text{-Co}_3\text{O}_4$ ) were prepared using modified versions of published methods,<sup>34</sup> in which the total volume of  $n$ -decane added was increased to 25 cm<sup>3</sup>. Mesoporous cobalt oxide ( $m\text{-Co}_3\text{O}_4$ ) with CMK-3-type structure was obtained by modification of a previously reported nanocasting method that utilized short-channel SBA-15<sup>35</sup> as a sacrificial hard template (see SI for further synthetic details).

**Material Characterization.** PXRD of the  $\text{Ag}_x\text{Ir}_{(100-x)}$ NPs was performed on a Rigaku R-Axis Spider Diffractometer with a  $\text{CuK}_\alpha$  source ( $\lambda = 1.5406 \text{ \AA}$ ), operating at 1.6 kW. TEM samples were prepared by drop-casting ethanolic suspensions of the NPs onto copper grids (200 mesh Cu/Formvar; Ted Pella, Inc.) and allowing to evaporate in air. Low-resolution TEM images were collected on a FEI Tecnai Transmission Electron Microscope operating at 80 kV. High-resolution TEM images, EDS 2-D elemental mapping and line scans were performed on JEOL 2010F Transmission Electron Microscope. XPS spectra were collected using a Kratos X-ray Photoelectron Spectrometer fitted with a monochromated  $\text{AlK}_\alpha$  source ( $\lambda = 8.3386 \text{ \AA}$ ). Samples for XPS analysis were prepared by drop-casting ethanol solutions of the NPs onto indium–tin oxide (ITO) coated glass wafers and allowing complete evaporation of the solvent in air. ICP-OES samples were prepared by digesting the supported  $\text{Ag}_x\text{Ir}_{(100-x)}$ NPs catalysts in a CEM-MARS-5 microwave reactor at 200 °C for 2 h in a 1:3 (v:v) mixture of 30%  $\text{H}_2\text{O}_2$ /concentrated HCl. Bulk textural analyses of the support materials were performed using a Quantachrome IQ-1C gas analyzer.

**Model Catalysis Studies.** The  $\text{Ag}_x\text{Ir}_{(100-x)}$ NPs catalysts were prepared by deposition on supports via a wet impregnation method. The NPs were first dispersed in a 1:1 ethanol:water solution, then added dropwise to a suspension of the support ( $a\text{-SiO}_2$ ,  $a\text{-Co}_3\text{O}_4$  or  $m\text{-Co}_3\text{O}_4$ ) in proportions that targeted a nominal 2–3% total (Ag+Ir) metal loading. After stirring the mixture for 20 min and a further sonication for 20 min, the solids were isolated by vacuum filtration or centrifugation and dried in a convection oven for 12 h at 70 °C. The actual metal loadings obtained were then analyzed by ICP-OES.

In a typical CHE hydrogenation catalysis study, ca. 3 mg of the  $\text{Ag}_x\text{Ir}_{(100-x)}/a\text{-SiO}_2$  catalyst was mixed with ca. 100 mg acid-washed and precalcined sand and loaded into a U-shaped borosilicate glass tube, suspended above a D3-porosity frit. The tube was suspended in a water bath held at 25 °C using an external circulating chiller. In a typical CRAL hydrogenation study, 16–18 mg of the  $\text{Ag}_x\text{Ir}_{(100-x)}/a\text{-Co}_3\text{O}_4$  or  $\text{Ag}_x\text{Ir}_{(100-x)}/m\text{-Co}_3\text{O}_4$  catalyst was mixed with ca. 200 mg of sand and loaded into a U-tube. The catalyst bed was heated to 200 °C using a heating blanket under an atmosphere of  $\text{H}_2/\text{He}$  for 12 h to release the PVP polymer from the NP surfaces. The reactor was then cooled to 90 °C and allowed to reach a static temperature before the reaction commenced. A glass container fitted with fritted bubbler containing either CHE or CRAL submerged in an ice bath at 0 °C was used to introduce a constant stream of reactant vapor into the gas stream. To initiate the reaction,  $\text{H}_2/\text{He}$  carrying the saturated substrate vapor was directed through the catalyst bed. The products were directly monitored on-stream by direct venting into an HP Agilent 6890 GC fitted with a 15 m Restex Stabilwax column and dual FID and TCD

detectors. Details of data workup to obtain catalyst activities and TOF values are provided in the SI.

**Computational Methodology.** All binding energies were calculated by DFT using the Vienna Ab Initio Simulation Package.<sup>36</sup> Electron correlation was evaluated within the generalized gradient approximation (GGA) via the Perdew–Burke–Ernzerhof (PBE) method.<sup>37</sup> For the valence electrons, Kohn–Sham wave functions were expanded in a plane wave basis set with an energy cutoff of 300 eV.<sup>38</sup> Core electrons were described via the projector augmented-wave method.<sup>39</sup> Geometries were considered optimized when the force on each atom was lower than 0.01 eV  $\text{\AA}^{-1}$ . Full details of calculations and kinetic modeling are given in the SI.

## ■ ASSOCIATED CONTENT

### 📄 Supporting Information

The Supporting Information is available free of charge on the ACS Publications website at DOI: 10.1021/acscatal.8b02103.

Detailed experimental and computational methods, further PXRD patterns, TEM images, XPS results, EDS spectra for the  $\text{Ag}_x\text{Ir}_{(100-x)}$ NPs, TEM images for the supports and composite catalysts, activation energy calculations for the  $\text{Ag}_x\text{Ir}_{(100-x)}/a\text{-SiO}_2$  catalysts, and additional catalysis, DFT, and modeled configuration information (PDF)

## ■ AUTHOR INFORMATION

### Corresponding Authors

\*E-mail: [henkelman@utexas.edu](mailto:henkelman@utexas.edu) (G.H.).

\*E-mail: [smh@cm.utexas.edu](mailto:smh@cm.utexas.edu) (S.M.H.).

### ORCID

Karalee Jarvis: 0000-0002-3560-0239

Haiqin Wan: 0000-0003-0639-4576

Graeme Henkelman: 0000-0002-0336-7153

Simon M. Humphrey: 0000-0001-5379-4623

### Present Address

<sup>§</sup>School of Environment, Nanjing University, 163 Xianlin Ave., Nanjing, Jiangsu 210023, China.

### Notes

The authors declare no competing financial interest.

## ■ ACKNOWLEDGMENTS

The authors thank Dr. Vincent M. Lynch (X-ray), Dr. Hugo Celio (XPS), and Dr. Dwight Romanovicz (TEM) for analytical assistance. Funding for this work was provided by the National Science Foundation under Grant Nos. CHE-1505135 & CHE-1807847 and the Welch Foundation (F-1738 & F-1841).

## ■ REFERENCES

- (1) Renner, H.; Schlamp, G.; Kleinwächter, I.; Drost, E.; Lüscho, H. M.; Tews, P.; Panster, P.; Diehl, M.; Lang, J.; Kreuzer, T.; Knödler, A.; Starz, K. A.; Dermann, K.; Rothaut, J.; Drieselmann, R. Platinum Group Metals and Compounds. In *Ullmann's Encyclopedia of Industrial Chemistry*; Wiley-VCH: Weinheim, Germany, 2012; Vol 28, pp 317–388.
- (2) (a) Adams, C. Applied Catalysis: A Predictive Socioeconomic History. *Top. Catal.* **2009**, *52*, 924–934. (b) Haynes, A.; Maitlis, P. M.; Morris, G. E.; Sunley, G. J.; Adams, H.; Badger, P. W.; Bowers, C. M.; Cook, D. B.; Elliott, P. I.; Ghaffar, T.; Green, H.; Griffin, T. R.; Payne, M.; Pearson, J. M.; Taylor, M. J.; Vickers, P. W.; Watt, R. J. Promotion of Iridium-Catalyzed Methanol Carbonylation: Mechanistic Studies of the Cativa Process. *J. Am. Chem. Soc.* **2004**, *126*, 2847–2861.

(c) Howard, M. J.; Sunley, G. J.; Poole, A. D.; Watt, R. J.; Sharma, B. K. New Acetyls Technologies from BP Chemicals. *Stud. Surf. Sci. Catal.* **1999**, *121*, 61–68. (d) Sunley, G. J.; Watson, D. J. High Productivity Methanol Carbonylation Catalysis Using Iridium: the Cativa Process for the Manufacture of Acetic Acid. *Catal. Today* **2000**, *58*, 293–307.

(3) Shieh, T.-S.; Yeh, S.-T.; Chu, M.-T.; Huang, Y.-C.; Tseng, M.-R.; Liu, J.-M. A Three-Spectrum White Organic Light Emitting Diode Base on a New Red Organometallic Iridium Complexes. *Dig. Tech. Pap. - Soc. Inf. Disp. Int. Symp.* **2005**, *36*, 855–857.

(4) Yoshinari, T.; Sato, K.; Haneda, M.; Kintaichi, Y.; Hamada, H. Positive Effect of Coexisting SO<sub>2</sub> on the Activity of Supported Iridium Catalysts for NO Reduction in the Presence of Oxygen. *Appl. Catal., B* **2003**, *41*, 157–169.

(5) (a) Okumura, M.; Masuyama, N.; Konishi, E.; Ichikawa, S.; Akita, T. CO Oxidation below Room Temperature over Ir/TiO<sub>2</sub> Catalyst Prepared by Deposition Precipitation Method. *J. Catal.* **2002**, *208*, 485–489. (b) Huang, Y.; Wang, A.; Li, L.; Wang, X.; Su, D.; Zhang, T. Ir-in-Ceria<sup>†</sup>: A Highly Selective Catalyst for Preferential CO Oxidation. *J. Catal.* **2008**, *255*, 144–152. (c) Van den Broek, A. C. M.; van Grondelle, J.; van Santen, R. A. Determination of Surface Coverage of Catalysts: Temperature Programmed Experiments on Platinum and Iridium Sponge Catalysts after Low Temperature Ammonia Oxidation. *J. Catal.* **1999**, *185*, 297–306.

(6) (a) Zhao, Y.; Hernandez-Pagan, E. A.; Vargas-Barbosa, N. M.; Dysart, J. L.; Mallouk, T. E. A High Yield Synthesis of Ligand-Free Iridium Oxide Nanoparticles with High Electrocatalytic Activity. *J. Phys. Chem. Lett.* **2011**, *2*, 402–406. (b) Swierk, J. R.; McCool, N. S.; Saunders, T. P.; Barber, G. D.; Strayer, M. E.; Vargas-Barbosa, N. M.; Mallouk, T. E. Photovoltage Effects of Sintered IrO<sub>2</sub> Nanoparticle Catalysts in Water-Splitting Dye-Sensitized Photoelectrochemical Cells. *J. Phys. Chem. C* **2014**, *118*, 17046–17053.

(7) Xia, X.; Figueroa-Cosme, L.; Tao, J.; Peng, H.-C.; Niu, G.; Zhu, Y.; Xia, Y. Facile Synthesis of Iridium Nanocrystals with Well-Controlled Facets Using Seed-Mediated Growth. *J. Am. Chem. Soc.* **2014**, *136*, 10878–10881.

(8) (a) Higaki, T.; Kitazawa, H.; Yamazoe, S.; Tsukuda, T. Partially Oxidized Iridium Clusters within Dendrimers: Size-Controlled Synthesis and Selective Hydrogenation of 2-Nitrobenzaldehyde. *Nanoscale* **2016**, *8*, 11371–11374. (b) Mizugaki, T.; Nagatsu, Y.; Togo, K.; Maeno, Z.; Mitsudome, T.; Jitsukawa, K.; Kaneda, K. Selective Hydrogenation of Levulinic Acid to 1,4-Pentanediol in Water Using a Hydroxyapatite-Supported Pt-Mo Bimetallic Catalyst. *Green Chem.* **2015**, *17*, 5136–5139.

(9) Yussenko, K. V.; Bykova, E.; Bykov, M.; Gromilov, S. A.; Kurnosov, A. V.; Prescher, C.; Prakapenka, V. B.; Crichton, W. A.; Hanfland, M.; Margadonna, S.; Dubrovinsky, L. S. High-Pressure High-Temperature Stability of hcp-Ir<sub>x</sub>Os<sub>1-x</sub> (x = 0.50 and 0.55) Alloys. *J. Alloys Compd.* **2017**, *700*, 198–207.

(10) (a) Zahmakiran, M. Iridium Nanoparticles Stabilized by Metal Organic Frameworks (IrNPs@ZIF-8): Synthesis, Structural Properties and Catalytic Performance. *Dalton Trans.* **2012**, *41*, 12690–12696. (b) Mondloch, J. E.; Wang, Q.; Frenkel, A. I.; Finke, R. G. Development Plus Kinetic and Mechanistic Studies of a Prototype Supported-Nanoparticle Heterogeneous Catalyst Formation System in Contact with Solution: Ir(1,5-COD)Cl/γ-Al<sub>2</sub>O<sub>3</sub> and Its Reduction by H<sub>2</sub> to Ir(0)n/γ-Al<sub>2</sub>O<sub>3</sub>. *J. Am. Chem. Soc.* **2010**, *132*, 9701–9714.

(11) (a) Casciato, M. J.; Vastola, J. T.; Lu, J. C.; Hess, D. W.; Grover, M. A. Initial Experimental Design Methodology Incorporating Expert Conjecture, Prior Data, and Engineering Models for Deposition of Iridium Nanoparticles in Supercritical Carbon Dioxide. *Ind. Eng. Chem. Res.* **2013**, *52*, 9645–9653. (b) Zhu, Y.; Jang, S. H. A.; Tham, Y. H.; Algin, O. B.; Maguire, J. A.; Hosmane, N. S. An Efficient and Recyclable Catalytic System Comprising Nano-Iridium(0) and a Pyridinium Salt of *nido*-Carboranyldiphosphine for the Synthesis of One-Dimensional Boronate Esters via Hydroboration Reaction. *Organometallics* **2012**, *31*, 2589–2596.

(12) ASM Handbook. Vol. 3: Alloy Phase Diagrams, 10<sup>th</sup> ed.; ASM International: Materials Park, OH, 1992.

(13) (a) Strasser, P.; Koh, S.; Anniyev, T.; Greeley, J.; More, K.; Yu, C.; Liu, Z.; Kaya, S.; Nordlund, D.; Ogasawara, H.; Toney, M. F. Lattice-Strain Control of the Activity in Dealloyed Core-Shell Fuel Cell Catalysts. *Nat. Chem.* **2010**, *2*, 454–460. (b) Chen, M.; Kumar, D.; Yi, C. W.; Goodman, D. W. The Promotional Effect of Gold in Catalysis by Palladium-Gold. *Science* **2005**, *310*, 291–293. (c) Slanac, D. A.; Hardin, W. G.; Johnston, K. P.; Stevenson, K. J. Atomic Ensemble and Electronic Effects in Ag-Rich AgPd Nanoalloy Catalysts for Oxygen Reduction in Alkaline Media. *J. Am. Chem. Soc.* **2012**, *134*, 9812–9819. (d) Sneed, B. T.; Brodsky, C. N.; Kuo, C. H.; Lamontagne, L. K.; Jiang, Y.; Wang, Y.; Tao, F.; Huang, W.; Tsung, C. K. Nanoscale-Phase-Separated Pd-Rh Boxes Synthesized via Metal Migration: An Archetype for Studying Lattice Strain and Composition Effects in Electrocatalysis. *J. Am. Chem. Soc.* **2013**, *135*, 14691–14700. (e) Liu, H.; Nosheen, F.; Wang, X. Noble Metal Alloy Complex Nanostructures: Controllable Synthesis and Their Electrochemical Property. *Chem. Soc. Rev.* **2015**, *44*, 3056–3078.

(14) Bao, J.; Dou, M.; Liu, H.; Wang, F.; Liu, J.; Li, Z.; Ji, J. Composition-Dependent Electrocatalytic Activity of Palladium-Iridium Binary Alloy Nanoparticles Supported on the Multiwalled Carbon Nanotubes for the Electro-Oxidation of Formic Acid. *ACS Appl. Mater. Interfaces* **2015**, *7*, 15223–15229.

(15) (a) Singh, S. K.; Xu, Q. Bimetallic Nickel-Iridium Nanocatalysts for Hydrogen Generation by Decomposition of Hydrous Hydrazine. *Chem. Commun.* **2010**, *46*, 6545–6547. (b) Zhang, W.; Li, L.; Ding, W.; Chen, S.; Wang, H.; Wei, Z. A Solvent Evaporation Plus Hydrogen Reduction Method to Synthesize IrNi/C Catalysts for Hydrogen Oxidation. *J. Mater. Chem. A* **2014**, *2*, 10098–10103.

(16) (a) García, S.; Zhang, L.; Piburn, G. W.; Henkelman, G.; Humphrey, S. M. Microwave Synthesis of Classically Immiscible Rhodium-Silver and Rhodium-Gold Alloy Nanoparticles: Highly Active Hydrogenation Catalysts. *ACS Nano* **2014**, *8*, 11512–11521. (b) Kunal, P.; Li, H.; Dewing, B. L.; Zhang, L.; Jarvis, K.; Henkelman, G.; Humphrey, S. M. Microwave-Assisted Synthesis of Pd<sub>100-x</sub>Au<sub>x</sub> Alloy Nanoparticles: A Combined Experimental and Theoretical Assessment of Synthetic and Compositional Effects upon Catalytic Reactivity. *ACS Catal.* **2016**, *6*, 4882–4893. (c) Li, H.; Luo, L.; Kunal, P.; Bonifacio, C. S.; Duan, Z.; Yang, J. C.; Humphrey, S. M.; Crooks, R. M.; Henkelman, G. Oxygen Reduction Reaction on Classically Immiscible Bimetallics: A Case Study of RhAu. *J. Phys. Chem. C* **2018**, *122*, 2712–2716.

(17) (a) de la Hoz, A.; Diaz-Ortiz, A.; Moreno, A. Microwaves in Organic Synthesis. Thermal and non-Thermal Microwave Effects. *Chem. Soc. Rev.* **2005**, *34*, 164–178. (b) Rao, K. J.; Vaidhyanathan, B.; Ganguli, M.; Ramakrishnan, P. A. Synthesis of Inorganic Solids Using Microwaves. *Chem. Mater.* **1999**, *11*, 882–895. (c) Baghbazadeh, M.; Carbone, L.; Cozzoli, P. D.; Kappe, C. O. Microwave-Assisted Synthesis of Colloidal Inorganic Nanocrystals. *Angew. Chem., Int. Ed.* **2011**, *50*, 11312–11359. (d) Tsukahara, Y.; Higashi, A.; Yamauchi, T.; Nakamura, T.; Yasuda, M.; Baba, A.; Wada, Y. In Situ Observation of Nonequilibrium Local Heating as an Origin of Special Effect of Microwave on Chemistry. *J. Phys. Chem. C* **2010**, *114*, 8965–8970.

(18) Dahal, N.; García, S.; Zhou, J.; Humphrey, S. M. Beneficial Effects of Microwave-Assisted Heating versus Conventional Heating in Noble Metal Nanoparticle Synthesis. *ACS Nano* **2012**, *6*, 9433–9446.

(19) Fan, F.; Liu, D.; Wu, Y.; Duan, S.; Xie, Z.; Jiang, Z.; Tian, Z. Epitaxial Growth of Heterogeneous Metal Nanocrystals: From Gold Nano-octahedra to Palladium and Silver Nanocubes. *J. Am. Chem. Soc.* **2008**, *130*, 6949–6951.

(20) Schuette, W. M.; Buhro, W. E. Silver Chloride as a Heterogeneous Nucleant for the Growth of Silver Nanowires. *ACS Nano* **2013**, *7*, 3844–3853.

(21) Dean, J. A. *Lange's Handbook of Chemistry*; McGraw-Hill: New York, 1972.

(22) Xia, X.; Wang, Y.; Ruditskiy, A.; Xia, Y. 25th Anniversary Article: Galvanic Replacement: A Simple and Versatile Route to Hollow Nanostructures with Tunable and Well-Controlled Properties. *Adv. Mater.* **2013**, *25*, 6313–6333.

(23) (a) Watzky, M. A.; Finke, R. G. Transition Metal Nanocluster Formation Kinetic and Mechanistic Studies. A New Mechanism When

Hydrogen Is the Reductant: Slow, Continuous Nucleation and Fast Autocatalytic Surface Growth. *J. Am. Chem. Soc.* **1997**, *119*, 10382–10400. (b) Watzky, M. A.; Finke, R. G. Nanocluster Size-Control and “Magic Number” Investigations. Experimental Tests of the “Living-Metal Polymer” Concept and of Mechanism-Based Size-Control Predictions Leading to the Syntheses of Iridium(0) Nanoclusters Centering about Four Sequential Magic Numbers. *Chem. Mater.* **1997**, *9*, 3083–3095. (c) Watzky, M. A.; Finney, E. E.; Finke, R. G. Transition-Metal Nanocluster Size vs Formation Time and the Catalytically Effective Nucleus Number: A Mechanism-Based Treatment. *J. Am. Chem. Soc.* **2008**, *130*, 11959–11969. (d) Tao, A. R.; Habas, S.; Yang, P. Shape Control of Colloidal Metal Nanocrystals. *Small* **2008**, *4*, 310–325.

(24) Du, Y. K.; Yang, P.; Mou, Z. G.; Hua, N. P.; Jiang, L. Thermal Decomposition Behaviors of PVP Coated on Platinum Nanoparticles. *J. Appl. Polym. Sci.* **2006**, *99*, 23–26.

(25) Li, H.; Henkelman, G. Dehydrogenation Selectivity of Ethanol on Close-Packed Transition Metal Surfaces: A Computational Study of Monometallic, Pd/Au, and Rh/Au Catalysts. *J. Phys. Chem. C* **2017**, *121*, 27504–27510.

(26) Luo, L.; Duan, Z.; Li, H.; Kim, J.; Henkelman, G.; Crooks, R. M. Tunability of the Adsorbate Binding on Bimetallic Alloy Nanoparticles for the Optimization of Catalytic Hydrogenation. *J. Am. Chem. Soc.* **2017**, *139*, 5538–5546.

(27) Claus, P. Selective Hydrogenation of  $\alpha,\beta$ -Unsaturated Aldehydes and Other C=O and C=C Bonds Containing Compounds. *Top. Catal.* **1998**, *5*, 51–62.

(28) (a) Zanella, R.; Louis, C.; Giorgio, S.; Touroude, R. Crotonaldehyde Hydrogenation by Gold Supported on TiO<sub>2</sub>: Structure Sensitivity and Mechanism. *J. Catal.* **2004**, *223*, 328–339. (b) Freakley, S. J.; He, Q.; Harrhy, J. H.; Lu, L.; Crole, D. A.; Morgan, D. J.; Ntainjua, E. N.; Edwards, J. K.; Carley, A. F.; Borisevich, A. Y.; Kiely, C. J.; Hutchings, G. J. Palladium-Tin Catalysts for the Direct Synthesis of H<sub>2</sub>O<sub>2</sub> with High Selectivity. *Science* **2016**, *351*, 965–968. (c) Matsubu, J. C.; Zhang, S.; DeRita, L.; Marinkovic, N. S.; Chen, J.; Graham, G. W.; Pan, X.; Christopher, P. Adsorbate-Mediated Strong Metal-Support Interactions in Oxide-Supported Rh Catalysts. *Nat. Chem.* **2017**, *9*, 120–127. (d) Li, S.; Xu, Y.; Chen, Y.; Li, W.; Lin, L.; Li, M.; Deng, Y.; Wang, X.; Ge, B.; Yang, C.; Yao, S.; Xie, J.; Li, Y.; Liu, X.; Ma, D. Tuning the Selectivity of Catalytic Carbon Dioxide Hydrogenation over Iridium/Cerium Oxide Catalysts with a Strong Metal-Support Interaction. *Angew. Chem., Int. Ed.* **2017**, *56*, 10761–10765.

(29) Kennedy, G.; Melaet, G.; Han, H.; Ralston, W. T.; Somorjai, G. A. In Situ Spectroscopic Investigation into the Active Sites for Crotonaldehyde Hydrogenation at the Pt Nanoparticle-Co<sub>3</sub>O<sub>4</sub> Interface. *ACS Catal.* **2016**, *6*, 7140–7147.

(30) Rumpelcker, A.; Kleitz, F.; Salabas, E.-L.; Schüth, F. Hard Templating Pathways for the Synthesis of Nanostructured Porous Co<sub>3</sub>O<sub>4</sub>. *Chem. Mater.* **2007**, *19*, 485–496.

(31) Brunauer, S.; Emmett, P. H.; Teller, E. Adsorption of Gases in Multimolecular Layers. *J. Am. Chem. Soc.* **1938**, *60*, 309–319.

(32) Barrett, E. P.; Joyner, L. G.; Halenda, P. P. The Determination of Pore Volume and Area Distributions in Porous Substances. I. Computations from Nitrogen Isotherms. *J. Am. Chem. Soc.* **1951**, *73*, 373–380.

(33) Reyes, P.; Aguirre, M. C.; Pecchi, G.; Fierro, J. L. G. Crotonaldehyde Hydrogenation on Ir Supported Catalysts. *J. Mol. Catal. A: Chem.* **2000**, *164*, 245–251.

(34) Dahal, N.; Ibarra, I. A.; Humphrey, S. M. High Surface Area Mesoporous Co<sub>3</sub>O<sub>4</sub> from a Direct Soft Template Route. *J. Mater. Chem.* **2012**, *22*, 12675–12681.

(35) Zhao, D.; Feng, J.; Huo, Q.; Melosh, N.; Fredrickson, G. H.; Chmelka, B. F.; Stucky, G. D. Triblock Copolymer Syntheses of Mesoporous Silica with Periodic 50 to 300 Angstrom Pores. *Science* **1998**, *279*, 548–552.

(36) Kresse, G.; Furthmüller, J. Efficient Iterative Schemes for *ab initio* Total-Energy Calculations Using a Plane-Wave Basis Set. *Phys. Rev. B: Condens. Matter Mater. Phys.* **1996**, *54*, 11169–11186.

(37) Perdew, J. P.; Burke, K.; Ernzerhof, M. Generalized Gradient Approximation Made Simple. *Phys. Rev. Lett.* **1996**, *77*, 3865–3868.

(38) Kohn, W.; Sham, L. Self-Consistent Equations Including Exchange and Correlation Effects. *Phys. Rev.* **1965**, *140*, A1133–A1138.

(39) Blöchl, P. E. Projector Augmented-Wave Method. *Phys. Rev. B: Condens. Matter Mater. Phys.* **1994**, *50*, 17953–17979.